Contents lists available at ScienceDirect

Microporous and Mesoporous Materials

journal homepage: www.elsevier.com/locate/micromeso

From natural clay minerals to porous silicon nanoparticles

Qingze Chen[a,b], Runliang Zhu[a,*], Haoyang Fu[a,b], Lingya Ma[a], Jianxi Zhu[a], Hongping He[a], Youjun Deng[c]

[a] CAS Key Laboratory of Mineralogy and Metallogeny, Guangdong Provincial Key Laboratory of Mineral Physics and Material, Guangzhou Institute of Geochemistry, Chinese Academy of Sciences, Guangzhou 510640, China
[b] University of Chinese Academy of Sciences, Beijing 100049, China
[c] Department of Soil and Crop Sciences, Texas A & M University College Station, TX 77843, United States

ARTICLE INFO

ABSTRACT

Nanostructured silicon has gained increasing interests due to its unique properties and wide applications. A facile, low-cost, and scalable strategy for producing nanostructured silicon remains a challenge. In this work, three natural clay minerals with different nanostructures, i.e., tabular halloysite, layered montmorillonite, and chain-layered palygorskite, were directly employed as precursors to synthesize porous nanostructured silicon via a combination of molten salt and magnesiothermic reduction. Results indicated that molten salt could efficiently absorb the massive heat generated from the exothermic reaction, which consequently inhibited the formation of high temperature phases (i.e., spinel and mullite) and the fusion of the generated silicon nanoparticles. Apart from acting as a reductant, metal Mg also consumed a part of the released heat through its vaporization to further lower the local reaction temperature. As a result, the as-synthesized nanostructured silicon showed large specific surface areas and enhanced porous architectures, e.g., 115.5 m^2/g of specific surface area and 0.547 cm^3/g of porosity for the sample obtained from palygorskite. Moreover, the microstructure and morphology of the resulting nanostructured silicon could be readily adjusted by properly choosing the clay mineral precursors and the added amounts of NaCl and Mg. Our strategy does not need to specially eliminate Al in clay minerals before reduction reaction, and greatly broadened the selection of clay minerals that can be directly used as silicon precursors, which would be beneficial to the practical production and wide applications of nanostructured silicon.

1. Introduction

Nanostructured silicon has gained significant attentions due to their unique properties and potential applications in many fields, including energy science (e.g., anodes for lithium-ion batteries and catalysts for hydrogen evolution) [1–3], environmental remediation (e.g., chemical sensors and heterogeneous catalysts) [4,5], and biomedicine (e.g., biological imaging and drug delivery) [6,7]. Compared with bulk silicon, nanostructured silicon can provide larger surface areas for target reactions or anchoring active materials, facilitate the interfacial transport process, and shorten the diffusion distance [8,9]. The enhanced void spaces within the nanostructures can effectively accommodate the volume change of silicon and suppress the diffusion-induced strain during some specific reactions (e.g., lithiation/delithiation during the charge-discharge cycles) [10,11].

Diverse silicon nanostructures (e.g., nanoparticles [12,13], nanowires [14–16], nanosheets [17,18], and porous structures [19,20]) have

been successfully synthesized with numerous methods, such as chemical vapor deposition [16], chemical reduction [17], and metal-assisted chemical etching [15]. Among these methods, magnesiothermic reduction has been considered as a promising method to fabricate nanostructured silicon due to a facile and low-energy experimental process [21,22]. In the previous studies, silica [23], silane [24], and silicon-containing polymers [21], which are essentially derived from quartzite, have been used as the silicon precursors. The preparation of silicon nanostructures generally involved the utilization of templates (e.g., polyethyleneimine and polyacrylonitrile) [25,26] or noble metal catalysts [16]. The complex preparation process and high cost of these silicon precursors have prohibited their applications in practice. Several studies also used the natural plant derivatives (e.g., rice husks [27] and reed leaves [28]) as sustainable silicon sources. However, the low silicon content in the precursors greatly limited the final yield. As such, exploring environmentally-friendly and low-cost precursors for scalable synthesis of nanostructured silicon is of high interest.

With natural micro/nano-sized structures, high silicon content, and abundant supplies [29,30], using clay minerals as precursors for synthesizing porous silicon nanoparticles are drawing increasing attentions recently [31,32]. Several studies have demonstrated that clay minerals could be used as precursors to synthesize nanostructured silicon *via* magnesiothermic reduction [31,32]. As the large amount of elemental Al in Al-containing clay minerals may combine with magnesium- or silicon-oxygen compounds during the highly exothermic magnesiothermic reaction to generate unwanted byproducts (e.g., spinel or mullite), the clay minerals (e.g., halloysite (Hal) and palygorskite (Pal)) were generally firstly converted into amorphous SiO_2 by selective acid etching before the magnesiothermic reduction reactions [32,33]. This process obviously will make the synthesis process complex and costly. A few studies also directly chose Al-free clay minerals (e.g., talc and Laponite) as the precursors [31,34], but this strategy will greatly limit the selection of clay minerals that can be used as silicon precursors, as Al-containing clay minerals (e.g., montmorillonite (Mt) and kaolinite) account for a major proportion in the family of clay minerals [30].

On the other hand, salt melt synthesis has proven to be a significant approach in the synthesis of nanoparticles (e.g., semiconductors and carbon nanomaterials) [35,36]. Molten salts could provide a controllable high-temperature liquid environment with chemical stability and low vapor pressure, and have the advantage of isolation of the resulting products [35,36]. With respect to the synthesis of nanostructured silicon *via* magnesiothermic reduction, molten salts might be able to scavenge the massive heat generated from the exothermic process. Consequently, the reaction temperature could be lowered to a moderate degree, which may avoid the formation of high temperature phases. As such, we hypothesize that Al-containing clay minerals without pretreatment may be directly used to synthesize nanostructured silicon by a combination of molten salt and magnesiothermic reduction. Furthermore, by properly choosing clay mineral precursors and the added amounts of molten salt and Mg, we expect this strategy may readily adjusting the microstructure and morphology of the resulting nanostructured silicon.

In the present work, three Al-containing clay minerals with different nanostructures, i.e., tubular Hal (tubule_Hal), layered Mt (layer_Mt), and chain-layered Pal (chain_Pal), were selected as precursors to fabricate porous silicon nanoparticles *via* molten salt-assisted magnesiothermic reduction reaction. The influences of the clay mineral precursors and the added amounts of Mg and NaCl on the structure and morphology of the resulting silicon were investigated. We expect the molten salt (i.e., NaCl) would feature three functions, i.e., serving as a heat scavenger for the exothermic reaction, as a dispersing agent for the silicon nanoparticles, and (specially, for layer_Mt) as an intercalation agent for the exfoliation of montmorillonite layers.

2. Materials and methods

2.1. Materials

The pristine tubule_Hal used in this study was from Shanxi, China. The sample was purified *via* the sedimentation method, dried overnight at 80 °C, and collected (purity > 98%) for the following experiments. The raw calcium-rich layer_Mt (purity > 95%) obtained from Inner Mongolia and chain_Pal (purity > 93%) from Anhui, China, were used as received without any further purification. The structures of these three clay minerals were illustrated in Fig. 1. Magnesium (Mg) and NaCl were of analytical grades and supplied by Tianjin Fuchen Chemical Reagents Factory and Shanghai RichJoint Chemical Reagents Co. Ltd, respectively. The HCl (37 wt%) and HF (40 wt%) were purchased from Guangzhou Chemical Reagent Factory, China.

2.2. Synthesis of the silicon nanoparticles

The silicon nanoparticles were prepared *via* the combined

magnesiothermic reduction and salt melt system and subsequent acid washing process. Typically, tubule_Hal was uniformly mixed with Mg powder and NaCl in a mass ratio of 1: x: y (x = 0.7, 0.8, and 0.9; y = 0, 3, and 5). The mixture was then loaded into a high-temperature and high-pressure stainless steel reactor, followed by transferring to an alumina tube furnace and heating at 650 °C for 5 h under a high-purity Ar flow. The resultant products were first washed with distilled water to eliminate NaCl (which could be recycled *via* evaporating the filtrate). Subsequently, 1 mol/L HCl were employed to remove generated MgO and other possible impurities (e.g., Mg_2Si, byproduct of the reaction between Si and excess Mg). Finally, the products were leached with 1% HF, and rinsed with distilled water, and then vacuum-dried at 60 °C for 12 h.

The silicon nanoparticle synthesized in a mass ratio of tubule_Hal: Mg: NaCl = 1: 0.8: 0 was denoted as Si(Hal80) and the others were denoted in the same way. Layer_Mt and chain_Pal were conducted under the same experimental conditions as tubule_Hal, and accordingly the final silicon nanoparticles were denoted as Si(Mtxy) and Si(Palxy), respectively. Detailed explanations of the abbreviations for the samples are given in Table S1.

2.3. Characterization methods

The powder X-ray diffraction (XRD) patterns of the samples were recorded on a Bruker D8 Advance X-ray diffractometer (Bruker AXS, Germany) with Ni-filtered CuKα radiation (λ = 0.154 nm), operating at 40 kV and 40 mA. The patterns were recorded at a scanning rate of 3°/min over the range of 3–80° (2θ). Powdered samples were loaded into the sample support and pressed smoothly before measurement.

Raman spectra were carried out on a Renishaw 2000 Microscopic confocal Raman Spectrometer (Renishaw, UK) equipped with an air-cooled CCD detector and an Ar-ion laser (λ = 514.5 nm). All measurements were conducted under the same experimental conditions (a laser power of 2 mW, 30-s acquisition time, and a 50 × magnification objective), and the spectra were recorded over the wavelength range of 200–1200 cm^{-1} with a resolution of 2 cm^{-1}.

The X-ray photoelectron spectroscopy (XPS) analysis was conducted on a Thermo Fisher K-Alpha XPS instrument (Thermo Fisher Scientific, UK) with a monochromatic AlKα X-ray source (1468.6 eV). XPS spectra were collected using an X-ray spot size of 400 μm in an ultra-high vacuum (chamber pressure < 5 × 10^{-8} mbar). The pass energies for survey scans and high resolution scans were 100 and 30 eV, respectively, and the energy resolution was better than 0.5 eV.

The N_2 adsorption-desorption isotherms were performed at liquid nitrogen temperature (–196 °C) on an ASAP 2020 analyzer (Micromeritics Instrument Corp. USA). The samples were degassed under vacuum at 200 °C for 12 h prior to determination. The S_{BET} of the sample was obtained by the multi-point Brunauer–Emmett–Teller (BET) method, and adsorption points were selected in the relative pressure range from 0.05 to 0.20 [37,38]. The total pore volume (V_{total}) was evaluated from nitrogen adsorption at a relative pressure of 0.97, and the pore size distribution analysis was determined by the Barrett-Joyner-Halenda (BJH) method [38].

The scanning electron microscopy (SEM) micrographs were obtained using an SU8010 cold field emission scanning electron microscope (FESEM, Hitachi, Japan) attached with energy dispersive X-ray spectroscopy (EDS, AMETEK-EDAX, USA). The specimens for SEM observation were anchored tightly on the surface of the conducting tape, and then transferred directly into the microscope.

The transmission electron microscopy (TEM) and selected area electronic diffraction (SAED) were recorded on an FEI Talos F200S field-emission transmission electron microscope equipped with SAED attachments at an acceleration voltage of 200 kV. The specimens were ultrasonically dispersed in ethanol and then dropped onto a copper grid coated with carbon film before TEM observation.
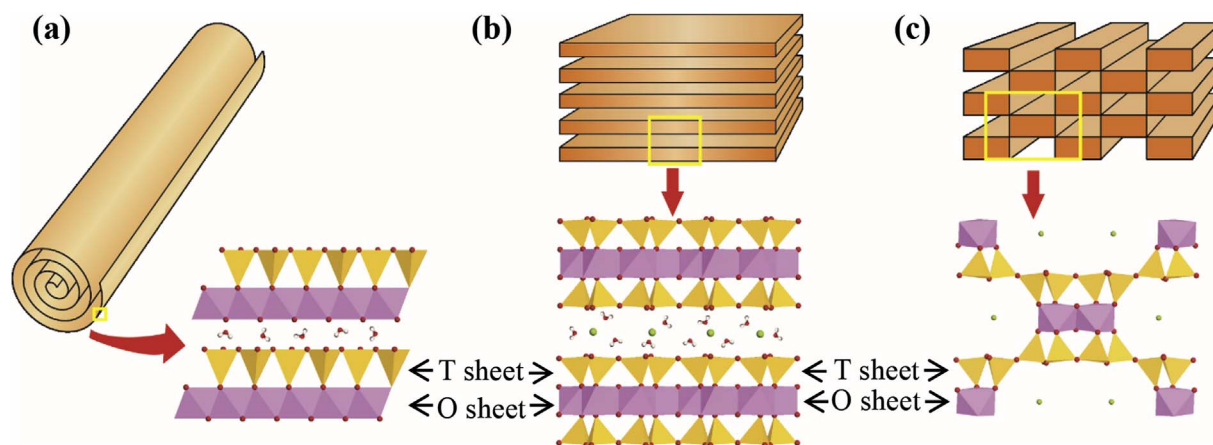
Fig. 1. Structures of tubule_Hal (a), layer_Mt (b), and chain_Pal (c). Those three clay minerals are phyllosilicates in which the individual layers are mainly composed of a tetrahedral (T) and a octahedral (O) sheet in either a 1:1 (Hal) or 2:1 (Mt and Pal) proportion. Due to isomorphous substitution (e.g., Al^{3+} for Si^{4+} in the T sheet and/or Mg^{2+} for Al^{3+} in the O sheet), the layers of many clay minerals (e.g., Mt and Pal) carry a permanent negative charge, which is balanced by exchangeable cationic within the interlayer space.

3. Results

The XRD patterns of the samples at different reaction stages were first recorded (Fig. 2). Tubule_Hal exhibited a characteristic (001) reflection of halloysite at ~11.76° (2θ), which corresponded to a d_{001}-value of 0.75 nm [39,40]. After the magnesiothermic reaction without NaCl (intermediate I), the characteristic reflections of Si and MgO were observed, suggesting that the silicon-oxygen tetrahedra of tubule_Hal have been reduced to silicon by Mg. Meanwhile, other byproducts (e.g., Mg_2Si and Al) formed, probably through the reactions: Si (s) + 2 Mg (s, g) → Mg_2Si (s) and Al_2O_3 (s) + 3 Mg (s, g) → 2Al (s, l) + 3MgO (s). The selective acid etching caused the emergence of the sharp reflections of Si in the XRD pattern of Si(Hal80). The characteristic reflections of spinel ($MgAl_2O_4$) and mullite ($3Al_2O_3·2SiO_2$) were also discernible [41]. These two high-temperature products could not be removed by acid washing, which may be the main reason that previous studies generally eliminated Al from the clay minerals before the heating

[32,33] or directly used Al-free clay minerals as precursors [31,34]. With the introduction of NaCl, the XRD patterns of the reduction product (intermediate II) exhibited similar reflections as intermediate I, with the exception of presence of sharp NaCl reflections. After selective acid treatment, only the characteristic reflections of silicon were found in the XRD patterns of Si(Hal85), indicating the presence of single-phase and well-crystallized silicon. Interestingly, the high temperature phases disappeared for Si(Hal85), which could be attributed to the decreased temperature of the reaction system caused by endothermic effect of the fusion of NaCl (ΔH_{fusion} = 28.8 kJ/mol) [42].

Both NaCl and Mg functioned as heat sink in the synthesis of nanostructured silicon. As shown by the XRD patterns (Fig. 3a), the high temperature phases gradually decreased as the added amount of NaCl increased. Specifically, spinel and mullite appeared for Si(Hal80), while only spinel for Si(Hal83) and neither for Si(Hal85). As the formation temperature of mullite was generally higher than that of spinel [41,43], this phenomenon indicated that the reaction temperature decreased with increasing salt quantity. Therefore, the high temperature phases could be used as temperature indicators to detect the local reaction temperature. When Mg quantity is low, distinct characteristic reflections of spinel appeared in the XRD patterns of Si(Hal65) (Figure S1). With the Mg quantity increasing, very weak characteristic reflections corresponding to spinel were still discernible for Si(Hal75), but not for Si(Hal85) and Si(Hal95) (Fig. 3b). Only Si was observed in the latter two samples. This finding suggested that the local reaction temperature decreased with increasing Mg quantity, which may be ascribed to the reason that vaporization of Mg (ΔH_{vap} = 148.2 kJ/mol) could absorb a part of heat and further lower the reaction temperature. As such, Mg also acted as a heat scavenger (similar to NaCl) besides serving as a reductant for the magnesiothermic reaction.

Raman spectra have been proved to be one of the most effective tools for studying the microstructure of nanomaterials [44–46]. Compared to the sharp Raman band arising from the fundamental phonon mode of monocrystalline silicon (~521 cm^{-1}), those of Si(Hal80) and Si(Hal85) broadened and red-shifted to ~514 and ~507 cm^{-1} (Fig. 4a), respectively, which could be attributed to the size-confinement effect [47,48]. Wang reported that the Raman-scattering bands of silicon nanowires could shift and broaden with decreasing diameter of silicon nanowires, and that the confinement effect became more evident when the diameter of silicon nanowires decreased [47]. As such, the lower Raman shift of Si(Hal85) than that of Si(Hal80) implied the smaller silicon nanoparticles for Si(Hal85). In addition, the Raman shifts of the final products obtained with different added amount of Mg did not show distinct difference (Fig. 4b).

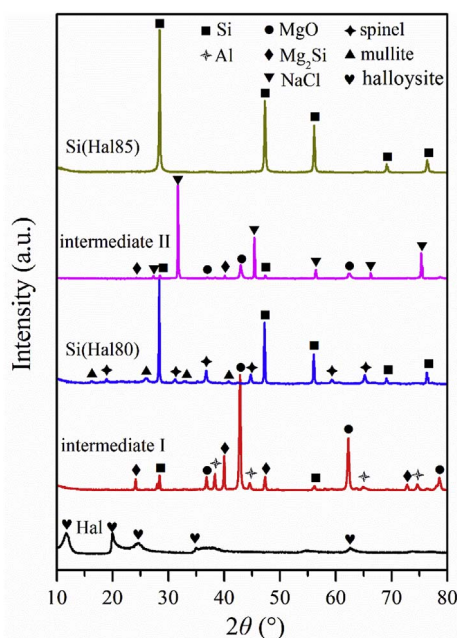The surface composition and chemical environment of

Fig. 2. XRD patterns of pristine tubule_Hal, the intermediate I (without NaCl) and intermediate II (with NaCl) after magnesiothermic reduction reaction, and the corresponding products after acid etching. Si(Hal80) and Si(Hal85) represent the final products synthesized in a mass ratio of tubule_Hal: Mg: NaCl = 1: 0.8: 0 and 1: 0.8: 5, respectively.
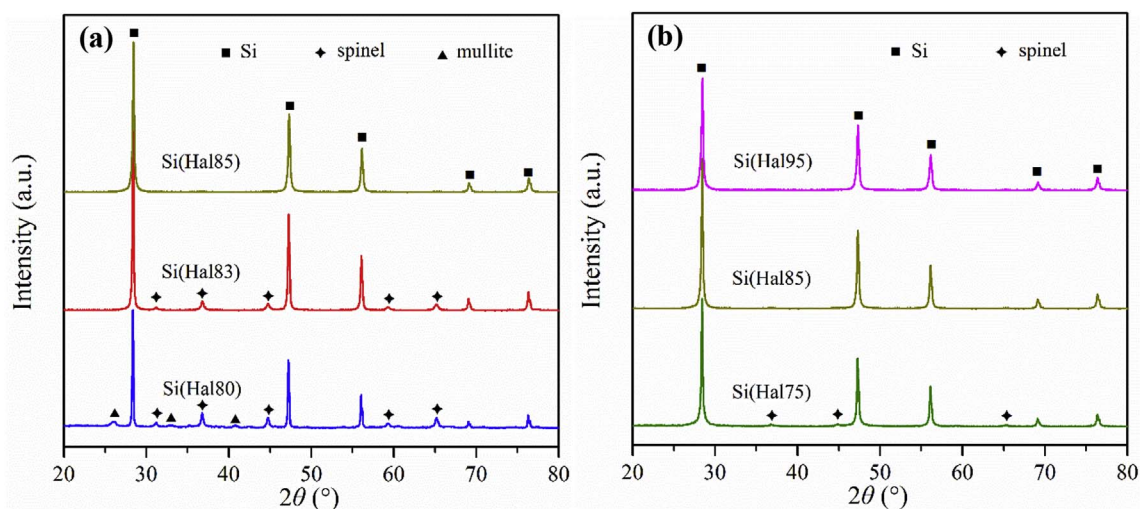
Fig. 3. XRD patterns of the final products obtained by changing the added amounts of NaCl (a) and Mg (b). The silicon nanoparticle synthesized in a mass ratio of tubule_Hal: Mg: NaCl = 1: 0.8: 0 was denoted as Si(Hal80) and the others were denoted in the same way.

nanostructured silicon were examined *via* XPS analysis. The XPS survey spectrum of nanostructured silicon (e.g., Si(Hal85)) revealed the existence of Si and O (Figure S2). The absence of metal elements indicated a high purity of the final product. The high-resolution Si 2p XPS spectra of silicon nanoparticles could be fitted into two major components centered at ∼99.3 and ∼99.9 eV, assigned to two peaks of Si (i.e., Si $2p_{3/2}$ and Si $2p_{1/2}$) (Fig. 4c). Besides, the silicon product displayed a weak peak at ∼103.1 eV, which could be attributed to a small amount of SiO_x derivatives [25,31]. The absence of SiO_2 peak at ∼103.4 eV resulting from the silicon-oxygen tetrahedral of pristine tubule_Hal (Figure S3) indicated the complete reaction of precursor during the reduction process. Therefore, the formed SiO_x species may result from the post-oxidation of the synthesized Si by exposure to air. Similar phenomena were reported in previous studies using other precursors to prepare nanoporous Si [31,49]. Moreover, both Si and SiO_x contents decreased with increasing the amount of reducing agent (Fig. 4c). Combining the XRD results, the excess Mg reacted with Si to generate Mg_2Si, which was easily removed by diluted HCl. As a result, increasing Mg quantity decreased Si yield. With respect to SiO_x species, the decrease of their content implied the lower content of post-oxidized Si, which may be due to the smaller S_{BET} of the final products.

The pristine tubule_Hal exhibited typical tubular shapes with a length of 0.2–1.0 μm and open-ended cylinders of halloysite nanotubes with a lumen diameter of ∼20 nm (Fig. 5a and b) [40,50]. The large crystals with little porous structure were visible in the SEM image of Si (Hal80) (Fig. 5c). In fact, the local reaction temperature in the magnesiothrmic reaction could reach over 1700 °C without any heat scavenger [51]. The massive heat thoroughly collapsed the pristine architectures of tubule_Hal and agglomerated the synthesized silicon nanoparticle into large crystals. In the case of NaCl as a heat scavenger, a rough surface and nanoporous structure with highly interconnected network could be clearly observed in obtained silicon (Fig. 5d–f). Apart from the role as a heat absorbent, NaCl also acted as a dispersing agent to prevent the synthesized silicon nanoparticles from agglomerating. Furthermore, the obtained silicon showed a poorly linked structure with increasing Mg quantity, probably due to the consumption of Si by excess Mg. The subsequent acid treatment disrupted the linkage of connected Si network as a result of the removal of the generated Mg_2Si. To further investigate the structural information of the silicon product, TEM and corresponding SAED pattern were carried out (Fig. 5g–i). TEM images of Si(Hal85) confirmed the interconnected silicon networks with the particle size from ∼50 nm to ∼100 nm (Fig. 5g). The crystal size of
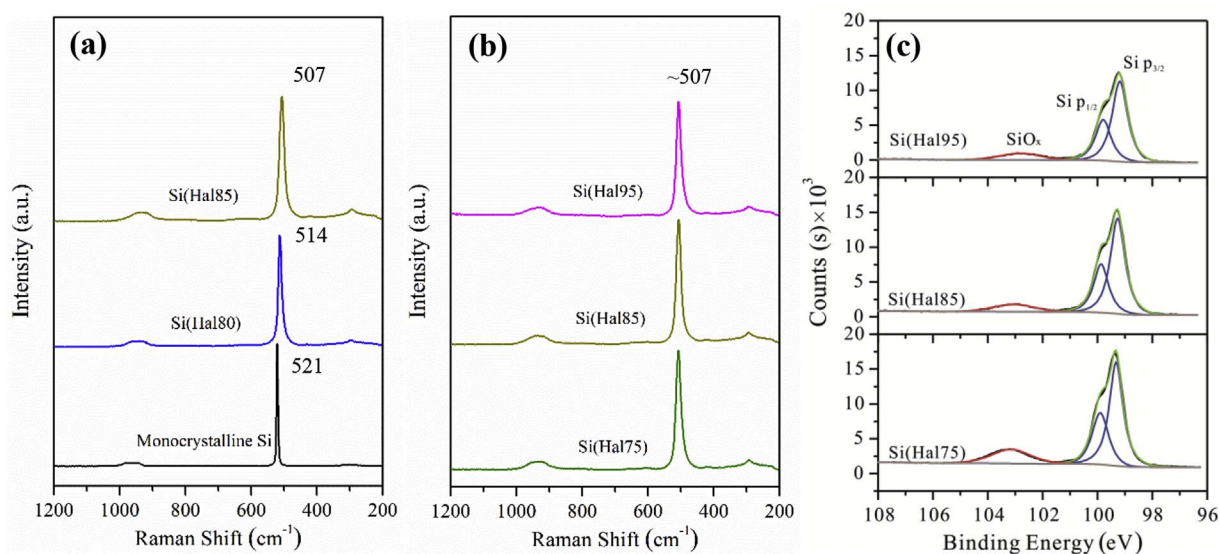

Fig. 4. Raman spectra of monocrystalline silicon and the silicon products (a and b); high reslution Si2p XPS spectra of the silicon products obtained with different added amount of Mg (c).
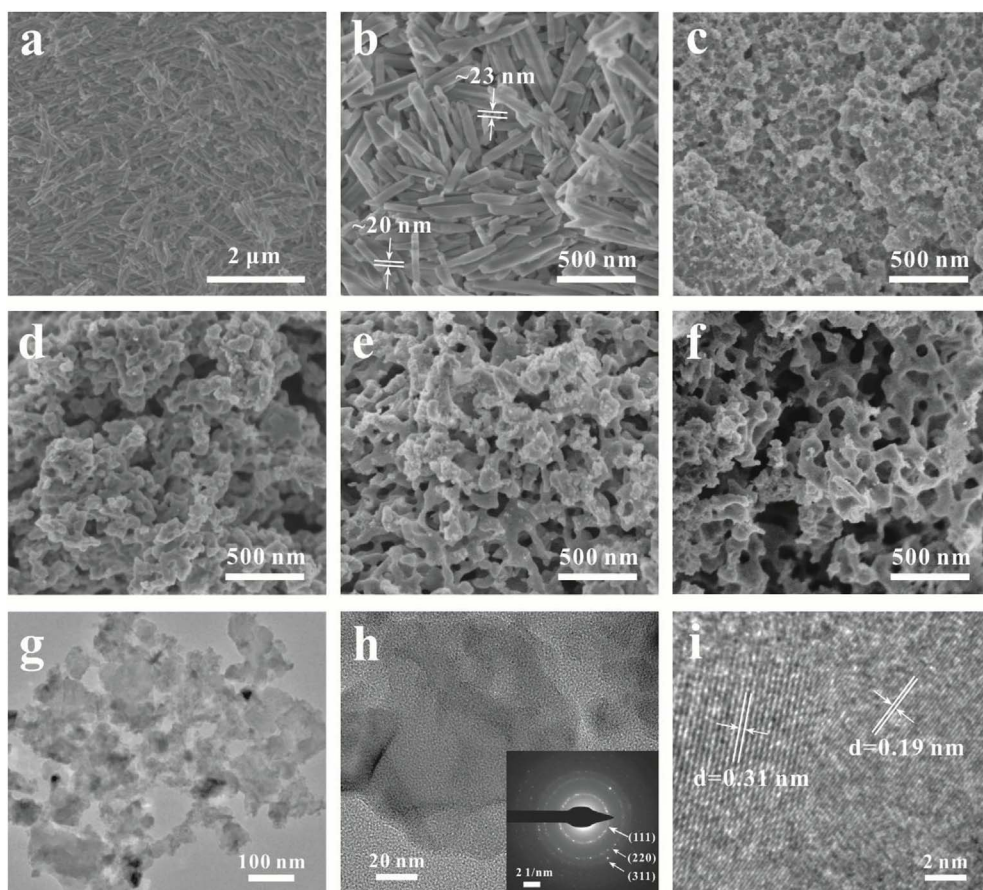
Fig. 5. SEM images of pristine tubule_Hal taken at low (a) and high (b) magnifications, Si(Hal80) (c), Si(Hal75) (d), Si(Hal85) (e), and Si(Hal95) (f). TEM image (g), HRTEM image (inset: corresponding SAED pattern) (h), magnified TEM image showing crystalline structure (i) of Si (Hal85).

Si(Hal85) was ~95 nm (Fig. 5h), which agreed well with the average value (~90 nm) calculated from the XRD pattern using the Scherrer equation. The SAED pattern showed diffraction rings indexed to crystalline Si (Fig. 5h), consistent with XRD results. The high-resolution TEM (HRTEM) image exhibited the interplanar spacings of ~0.31 and ~0.19 nm (Fig. 5i), corresponding to the (111) and (220) crystal planes of crystalline Si, respectively, which further confirmed the formation of Si nanocrystals. In addition, the bulk composition of Si(Hal85) calculated from EDS analysis clearly showed that the pure silicon product was obtained after acid washing (Table S2), consistent with the XPS survey spectra results above.

The pristine tubule_Hal possessed IV-type isotherm with H3 hysteresis loop (Fig. 6), indicative of slit-like pores of layered structure, according to the IUPAC technical report [38]. The slit-like pores with a size of several nanometers might be ascribed to the newly formed mesopores from the separation of rolled layers of tubule_Hal during dehydration process [52]. Si(Hal80) exhibited very small adsorption capacity of N_2 with a low S_{BET} value (~7.8 m^2/g) and a tiny V_{total} (~0.050 cm^3/g) (Table 1), manifesting a very dense product. In contrast, all the silicon nanoparticles obtained by NaCl-assisted reduction reaction had much greater N_2 adsorption capacity in the whole pressure range, particularly in the high relative pressures region, indicating the significant increase of meso- and macropores. The comparison of pore size distribution patterns further confirmed the improved porosity for the silicon nanoparticles in the case of NaCl (Figure S4). Accordingly, the calculated S_{BET} value and V_{total} of the silicon nanoparticles enhanced evidently in comparison with those of Si(Hal80) (Table 1). In addition, increasing Mg quantity slightly decreased the S_{BET} value and V_{total} of silicon nanoparticles (Table 1), which may be attributed to the destruction of micro- and mesopores by the side reaction between Si and Mg. On the other hand, the smaller S_{BET} for silicon nanoparticles implied lower surface areas exposed to air, and accordingly led to a
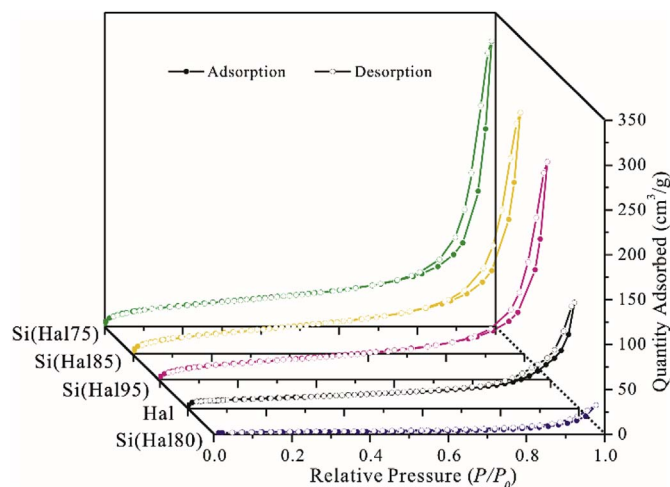

Fig. 6. N_2 adsorption-desorption isotherms of pristine tubule_Hal and the silicon products (i.e., Si(Hal80), Si(Hal75), Si(Hal85), and Si(Hal95)).

lower content of post-oxidized Si, which agreed well with the XPS results.

When the clays layer_Mt and chain_Pal (Figure S5) were employed as precursors in the synthesis of porous silicon nanoparticles *via* the same approach as tubule_Hal, the XRD indicated the presence of spinel in both Si(Mt80) and Si(Pal80) without the introduce of NaCl during the synthesis (Fig. 7a). In contrast, only a single-phase silicon was observed for both Si(Mt85) and Si(Pal85) when NaCl was introduced. The presence of NaCl effectively inhibited the formation of high temperature phases, which confirmed the role of NaCl as a heat scavenger during the magnesiothrmic reactions. According to the crystal size

Table 1
Textural characteristics of the pristine clay minerals (i.e., tubule_Hal, layer_Mt, and chain_Pal) and the final silicon products (i.e., Si(Hal80), Si(Hal75), Si(Hal85), Si(Hal95), Si(Mt80), Si(Mt85), Si(Pal80), and Si(Pal85)).

	S_{BET} (m²/g)	V_{total} (cm³/g)	Average pore diameters (nm)
tubule_Hal	40.6	0.127	15.8
Si(Hal80)	7.8	0.050	25.9
Si(Hal75)	92.4	0.341	14.8
Si(Hal85)	79.8	0.255	13.6
Si(Hal95)	72.7	0.242	13.3
layer_Mt	66.1	0.111	6.7
Si(Mt80)	10.8	0.032	11.9
Si(Mt85)	83.3	0.295	15.1
chain_Pal	141.1	0.334	9.5
Si(Pal80)	9.2	0.034	14.9
Si(Pal85)	115.5	0.547	19.0

calculation by the Scherrer equation, Si(Mt85) and Si(Pal85) possessed average crystal sizes of ∼49 and ∼24 nm, respectively. Compared with the Raman bands of Si(Mt80) and Si(Pal80), those of Si(Mt85) and Si(Pal85) red-shifted, broadened, and became more asymmetrical (Fig. 7b), suggesting smaller domain size according to the size-confinement effect. The microarchitectures of the final silicon particles were further verified by the SEM and TEM images (Fig. 8). The typical lamellar texture and fibrous morphology could be visible in the SEM images of layer_Mt and chain_Pal (Fig. 8a and e), respectively [53,54]. After Mg reduction, both Si(Mt80) and Si(Pal80) displayed dense and agglomerate morpholgies (Fig. 8b and f), indicating the formation of large Si crystal during the high temperature reaction. However, quite different morphology features appeared with the introduction of NaCl during the synthesis process. Si(Mt85) showed a lamellar and nanoporous morphology, which somewhat preserved the original lamellar structure of Mt (Fig. 8c and d). As for Si(Pal85), a rough surface with loose and porous nanoparticles emerged (Fig. 8g and h). Accordingly, Si(Mt85) and Si(Pal85) had much larger S_{BET} and V_{total} (Table 1), calculated by their N₂ adsorption-desorption isotherms (Figure S6), than Si(Mt80) and Si(Pal80). As such, the porous silicon nanoparticles were also successfully synthesized using layer_Mt and chain_Pal as precursors *via* a simple salt-assisted magnesiothrmic reduction reaction. Noticeably, the morphologies and porosities of the resulting silicon nanoparticles from different clay minerals (i.e., tubule_Hal, layer_Mt and chain_Pal) greatly differed, which indicated that the characteristics of precursors had great influences on the resulting silicon nanoparticles.

4. Discussion

Based on the above observation, the reaction process and mechanism of the synthesis of porous silicon nanoparticles from natural clay minerals could be deduced as follow:

First, the natural nano-sized architectures (e.g., the nanoscale lumens and newly formed slit-like pores of tubule_Hal, the interlayer spaces of layer_Mt and the nanorods of chain_Pal) provided large silicon-oxygen surface, ensuring the direct contact with molten salt (NaCl) and reductant (Mg). Second, the liquid Mg in molten salt could provide ions and solvated electrons with high activity and strong reducing power, which could efficiently break the Si-O bond [23]. Unsaturated bonds of Si atoms randomly bonded with adjacent Si atoms to form nearly spherical particles due to the optimization of the surface energy. The aluminum-oxygen octahedral sheets of the clay minerals were transformed to amorphous Al_2O_3 at high temperature [41,55], which could act as isolation barrier inhibiting the random bonding of unsaturated bonds on Si atoms and somewhat keeping the original nanostructure. Third, the molten salt absorbed the massive heat to lower the local reaction temperature, consequently inhibiting the formation of high temperature phases and the fusion of generated silicon nanoparticles. Meantime, the molten salt could prevent silicon nanoparticles from forming to large agglomerates. Specially, for layer_Mt, the activated molten salt might enter the interlayer spaces for inducing the exfoliation of layers [56], ensuring a sufficient reduction reaction. Finally, apart from serving as reductant, Mg also acted as heat scavenger as NaCl. The vaporization of Mg atoms adsorbed a part of heat, further lowering the reaction temperature to an appropriate degree.

The above results demonstrated that natural Al-containing clay minerals could be used as precursors to synthesize the porous silicon nanoparticles *via* salt-assisted magnesiothermic reduction reaction. The resulting nanostructured silicon showed large specific surface areas and enhanced porous architectures. For example, Si(Pal85) in this work showed a S_{BET} of 115.5 m²/g, which is close to the value of silicon nanoparticles from amorphous SiO_2 after acid treatment of clay minerals [32,33], much larger than that of the 2D nanostructured silicon from exfoliated Laponite nanosheet (43 m²/g) [31]. In addition, the V_{total} of Si(Pal85) (0.547 cm³/g) was higher than that of the recently reported multiscale hyperporous silicon flake from talc (0.368 cm³/g) [34]. Numerous studies have confirmed that nanostructured silicon with large specific surface area and porous architecture may be a promising material in energy science and environmental remediation [57,58]. Moreover, the microstructure and morphology of
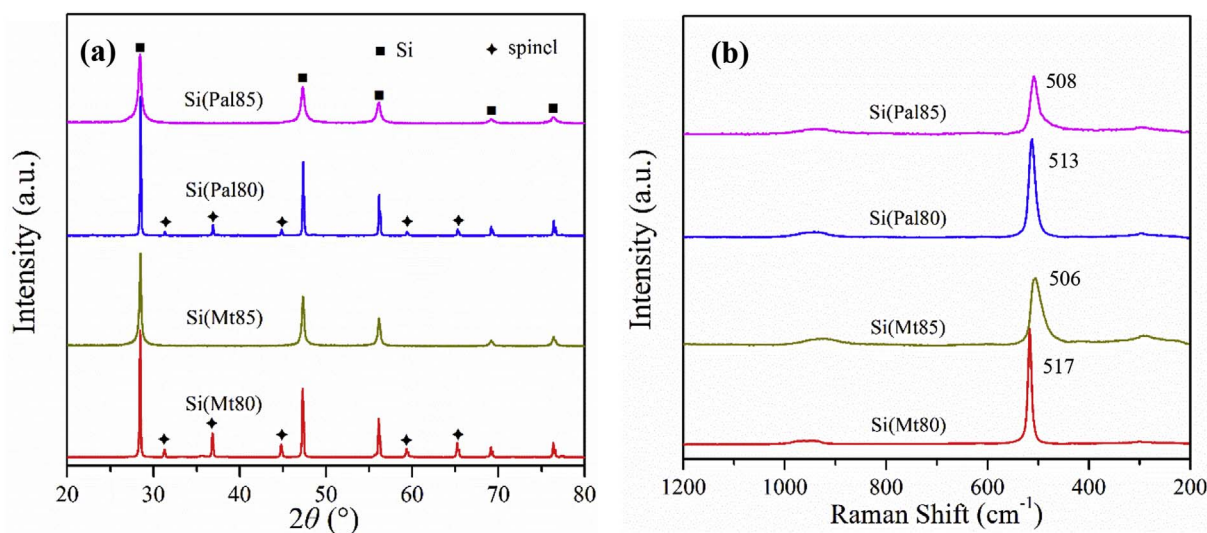

Fig. 7. XRD patterns (a) and Raman spectra (b) of the final products from pristine clay minerals (i.e., layer_Mt and chain_Pal) after magnesiothermic reduction reaction (without or with NaCl) and acid etching. The silicon nanoparticle synthesized in a mass ratio of layer_Mt: Mg: NaCl = 1: 0.8: 0 was denoted as Si(Mt80) and the others were denoted in the same way.
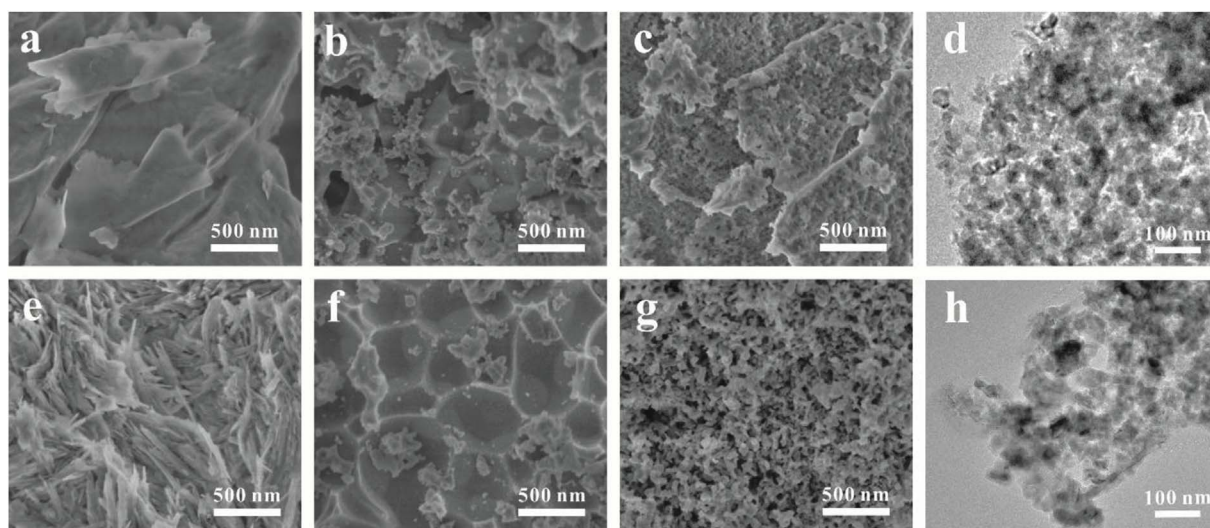
Fig. 8. SEM images of pristine layer_Mt (a), Si(Mt80) (b), Si(Mt85) (c), pristine chain_Pal (e), Si(Pal80) (f), and Si(Pal85) (g). TEM images of Si(Mt85) (d) and Si(Pal85) (h).

nanostructured silicon could be readily adjusted by properly choosing the appropriate precursors and the added amounts of NaCl and Mg. This strategy not only eliminated the time-consuming and complex pre-treatment process (e.g., selective acid etching or exfoliation) needed in previous studies, but also greatly extended the range of clay minerals used as silicon precursors, which could be beneficial to the large-scale production and practical applications of nanostructured silicon.

5. Conclusion

The porous silicon nanoparticles with large specific surface areas and enhanced porous architectures were successfully synthesized using Al-containing clay minerals (i.e., tubule_Hal, layer_Mt, and chain_Pal) *via* a combination of molten salt and magnesiothermic reduction. The results indicated that molten salt could efficiently absorb the massive heat, which consequently inhibited the formation of high temperature phases (i.e., spinel and mullite) and the fusion of generated silicon nanoparticles. Meanwhile, the molten salt could prevent the agglomeration of silicon nanoparticles, which aided in the synthesis of nanostructured silicon. Apart from acting as a reductant, metal Mg also adsorbed a part of heat through its vaporization to further lower the local reaction temperature. Moreover, by properly choosing the clay mineral precursors and the added amounts of NaCl and Mg, we could readily adjust the microstructure and morphology of the resulting nanostructured silicon. This work avoided complex pretreatment process employed in previous studies on the synthesis of nanostructured silicon, and greatly broadened the selection of clay minerals that can be directly used as silicon precursors, which would contribute to the practical production and wide applications of nanostructured silicon in various fields.

Appendix A. Supplementary data

Supplementary data related to this article can be found at http://dx.doi.org/10.1016/j.micromeso.2017.10.033.

References

[1] X. Su, Q.L. Wu, J.C. Li, X.C. Xiao, A. Lott, W.Q. Lu, B.W. Sheldon, J. Wu, Adv. Energy Mat. 4 (2014) 1–23.
[2] F. Dai, J.T. Zai, R. Yi, M.L. Gordin, H. Sohn, S.R. Chen, D.H. Wang, Nat. Commun. 5 (2014) 1–11.
[3] X.X. Zuo, J. Zhu, P. Muller-Buschbaum, Y.J. Cheng, Nano Energy 31 (2017) 113–143.
[4] F.A. Harraz, Sens. Actuat. B Chem. 202 (2014) 897–912.
[5] Y.M.A. Yamada, Y. Yuyama, T. Sato, S. Fujikawa, Y. Uozumi, Angew. Chem. Int. Ed. 53 (2014) 127–131.
[6] E.J. Henderson, A.J. Shuhendler, P. Prasad, V. Baumann, F. Maier-Flaig, D.O. Faulkner, U. Lemmer, X.Y. Wu, G.A. Ozin, Small 7 (2011) 2507–2516.
[7] Y.Y. Li, F. Cunin, J.R. Link, T. Gao, R.E. Betts, S.H. Reiver, V. Chin, S.N. Bhatia, M.J. Sailor, Science 299 (2003) 2045–2047.
[8] D.R. Rolison, J.W. Long, J.C. Lytle, A.E. Fischer, C.P. Rhodes, T.M. McEvoy, M.E. Bourg, A.M. Lubers, Chem. Soc. Rev. 38 (2009) 226–252.
[9] R. Liu, J. Duay, S.B. Lee, Chem. Commun. 47 (2011) 1384–1404.
[10] J.R. Szczech, S. Jin, Energy Environ. Sci. 4 (2011) 56–72.
[11] L.H. Liu, J. Lyu, T.H. Li, T.K. Zhao, Nanoscale 8 (2016) 701–722.
[12] C. Martin, O. Crosnier, R. Retoux, D. Bélanger, D.M. Schleich, T. Brousse, Adv. Funct. Mat. 21 (2011) 3524–3530.
[13] M.-H. Ryou, J. Kim, I. Lee, S. Kim, Y.K. Jeong, S. Hong, J.H. Ryu, T.-S. Kim, J.-K. Park, H. Lee, J.W. Choi, Adv. Mat. 25 (2013) 1571–1576.
[14] B.M. Bang, H. Kim, J.P. Lee, J. Cho, S. Park, Energy Environ. Sci. 4 (2011) 3395–3399.
[15] A. Vlad, A.L.M. Reddy, A. Ajayan, N. Singh, J.F. Gohy, S. Melinte, P.M. Ajayan, Natl. Acad. Sci. U. S. A. 109 (2012) 15168–15173.
[16] X. Li, J.-H. Cho, N. Li, Y. Zhang, D. Williams, S.A. Dayeh, S.T. Picraux, Adv. Energy Mat. 2 (2012) 87–93.
[17] W.-S. Kim, Y. Hwa, J.-H. Shin, M. Yang, H.-J. Sohn, S.-H. Hong, Nanoscale 6 (2014) 4297–4302.
[18] H. Nakano, T. Ikuno, Appl. Phys. Rev. 3 (2016) 040803.
[19] M.Y. Ge, J.P. Rong, X. Fang, A.Y. Zhang, Y.H. Lu, C.W. Zhou, Nano Res. 6 (2013) 174–181.
[20] Y. Yang, D.Q. Chen, B. Liu, J.B. Zhao, ACS Appl. Mat. Inter. 7 (2015) 7497–7504.
[21] R.Y. Zhang, Y.J. Du, D. Li, D.K. Shen, J.P. Yang, Z.P. Guo, H.K. Liu, A.A. Elzatahry, D.Y. Zhao, Adv. Mat. 26 (2014) 6749–6755.
[22] Z.H. Bao, M.R. Weatherspoon, S. Shian, Y. Cai, P.D. Graham, S.M. Allan, G. Ahmad, M.B. Dickerson, B.C. Church, Z.T. Kang, H.W. Abernathy III, C.J. Summers, M.L. Liu, K.H. Sandhage, Nature 446 (2007) 172–175.
[23] X.F. Liu, C. Giordano, M. Antonietti, J. Mat. Chem. 22 (2012) 5454–5459.
[24] N. Lin, Y. Han, L.B. Wang, J.B. Zhou, J. Zhou, Y.C. Zhu, Y.T. Qian, Angew. Chem. Int. Ed. 54 (2015) 3822–3825.
[25] X.L. Liu, Y.F. Gao, R.H. Jin, H.J. Luo, P. Peng, Y. Liu, Nano Energy 4 (2014) 31–38.
[26] J.-K. Yoo, J. Kim, Y.S. Jung, K. Kang, Adv. Mat. 24 (2012) 5452–5456.
[27] D.S. Jung, M.-H. Ryou, Y.J. Sung, S.B. Park, J.W. Choi, Natl. Acad. Sci. U. S. A. 110 (2013) 12229–12234.
[28] J. Liu, P. Kopold, P.A. van Aken, J. Maier, Y. Yu, Angew. Chem. Int. Ed. 54 (2015) 9632–9636.

[29] R.L. Zhu, Q.Z. Chen, Q. Zhou, Y.F. Xi, J.X. Zhu, H.P. He, Appl. Clay Sci. 123 (2016) 239–258.

[30] F. Bergaya, G. Lagaly, F. Bergaya, G. Lagaly (Eds.), Developments in Clay Science, 5A Elsevier, 2013, pp. 1–19 ch. 1.

[31] K. Adpakpang, S.B. Patil, S.M. Oh, J.-H. Kang, M. Lacroix, S.-J. Hwang, Electrochim. Acta 204 (2016) 60–68.

[32] X.Y. Zhou, L.L. Wu, J. Yang, J.J. Tang, L.H. Xi, B. Wang, J. Power Sources 324 (2016) 33–40.

[33] L. Sun, T.T. Su, L. Xu, H.-B. Du, Phys. Chem. Chem. Phys. 18 (2016) 1521–1525.

[34] J. Ryu, D. Hong, M. Shin, S. Park, ACS Nano 10 (2016) 10589–10597.

[35] X.F. Liu, N. Fechler, M. Antonietti, Chem. Soc. Rev. 42 (2013) 8237–8265.

[36] D.P. Chen, J. Fu, S.E. Skrabalak, Chem. Nano Mat. 1 (2015) 18–26.

[37] G.-P. Hao, G. Mondin, Z. Zheng, T. Biemelt, S. Klosz, R. Schubel, A. Eychmueller, S. Kaskel, Angew. Chem. Int. Ed. 54 (2015) 1941–1945.

[38] M. Thommes, K. Kaneko, A.V. Neimark, J.P. Olivier, F. Rodriguez-Reinoso, J. Rouquerol, K.S.W. Sing, Pure Appl. Chem. 87 (2015) 1051–1069.

[39] S.S. Zeng, C. Reyes, J.J. Liu, P.A. Rodgers, S.H. Wentworth, L.Y. Sun, Polymer 55 (2014) 6519–6528.

[40] P. Yuan, D.Y. Tan, F. Annabi-Bergaya, Appl. Clay Sci. 112–113 (2015) 75–93.

[41] Q.Z. Chen, R.L. Zhu, L.Y. Ma, Q. Zhou, J.X. Zhu, H.P. He, Appl. Clay Sci. 135 (2017) 129–135.

[42] B. Zalba, J.M. Marín, L.F. Cabeza, H. Mehling, Appl. Therm. Eng. 23 (2003) 251–283.

[43] Y. Safaei-Naeini, M. Aminzare, F. Golestani-Fard, Ceram. Int. 38 (2012) 841–845.

[44] Q.Z. Chen, H.M. Liu, R.L. Zhu, X. Wang, S.Y. Wang, J.X. Zhu, H.P. He, Micropor. Mesopor. Mat. 225 (2016) 137–143.

[45] N. Lin, J.B. Zhou, L.B. Wang, Y.C. Zhu, Y.T. Qian, ACS Appl. Mat. Inter. 7 (2015) 409–414.

[46] J. Mosa, M. Aparicio, A. Duran, C. Laberty-Robert, C. Sanchez, J. Mat. Chem. A 2 (2014) 3038–3046.

[47] R.P. Wang, G.W. Zhou, Y.L. Liu, S.H. Pan, H.Z. Zhang, D.P. Yu, Z. Zhang, Phys. Rev. B 61 (2000) 16827–16832.

[48] Z. Iqbal, S. Veprek, A.P. Webb, P. Capezzuto, Solid State Commun. 37 (1981) 993–996.

[49] Z.-W. Zhou, Y.-T. Liu, X.-M. Xie, X.-Y. Ye, Chem. Commun. 52 (2016) 8401–8404.

[50] X.K. Tian, W.W. Wang, Y.X. Wang, S. Komarneni, C. Yang, Micropor. Mesopor. Mat. 207 (2015) 46–52.

[51] B.H. Meekins, Y.-C. Lin, J.S. Manser, K. Manukyan, A.S. Mukasyan, P.V. Kamat, P.J. McGinn, ACS Appl. Mat. Inter. 5 (2013) 2943–2951.

[52] A. Fukami, Clay. Clay Min. 26 (1978) 25–40.

[53] Q.Z. Chen, R.L. Zhu, Y.P. Zhu, J. Liu, L.F. Zhu, L.Y. Ma, M. Chen, Appl. Clay Sci. 132 (2016) 412–418.

[54] E. Ruiz-Hitzky, M. Darder, A.C.S. Alcantara, B. Wicklein, P. Aranda, S. Kalia, Y. Haldorai (Eds.), Organic-inorganic Hybrid Nanomaterials, vol 267, 2015, pp. 39–86.

[55] L. Heller-Kallai, F. Bergaya, G. Lagaly (Eds.), Developments in Clay Science, vol. 5A, Elsevier, 2013, pp. 411–433 ch. 10.

[56] J. Ryu, Y.J. Jang, S. Choi, H.J. Kang, H. Park, J.S. Lee, S. Park, NPG Asia Mat. 8 (2016) 1–9.

[57] R. Yi, M.L. Gordin, D. Wang, Nanoscale 8 (2016) 1834–1848.

[58] F.-Y. Wang, Q.-D. Yang, G. Xu, N.-Y. Lei, Y.K. Tsang, N.-B. Wong, J.C. Ho, Nanoscale 3 (2011) 3269–3276.